



# Co-catalyst-free photocatalytic hydrogen evolution on TiO<sub>2</sub>: Synthesis of optimized photocatalyst through statistical material science



Yamen AlSalka<sup>a,b,\*</sup>, Amer Hakki<sup>c</sup>, Jenny Schneider<sup>a,b</sup>, Detlef W. Bahnemann<sup>a,b,d</sup>

<sup>a</sup> Institut für Technische Chemie, Leibniz Universität Hannover, Callinstr. 3, D-30167 Hannover, Germany

<sup>b</sup> Laboratorium für Nano- und Quantenengineering, Leibniz Universität Hannover, Schneiderberg 39, 30167 Hannover, Germany

<sup>c</sup> Department of Chemistry, University of Aberdeen, Meston Building, Meston Walk, AB24 3UE Aberdeen, Scotland, United Kingdom

<sup>d</sup> Laboratory "Photoactive Nanocomposite Materials", Saint-Petersburg State University, Ulyanovskaya str. 1, Peterhof, Saint-Petersburg, 198504, Russia

## ARTICLE INFO

**Keywords:**  
Photocatalysis  
Molecular hydrogen evolution  
TiO<sub>2</sub>  
Design of experiment  
EISA

## ABSTRACT

An active TiO<sub>2</sub> for co-catalyst-free photocatalytic hydrogen evolution was successfully synthesized employing a simple Evaporation-Induced Self-Assembly (EISA) method that was developed and optimized with the help of Design of Experiment (DoE) coupled with Full Factorial Design (FFD) methodology. Coupling DoE with FFD provides a statistical tool for optimizing the synthesis process while carrying out the smallest number of experiments. This tool builds a statistical framework to determine the significance of the studied factors, i.e., titanium-precursor type, surfactant type and surfactant quantity, along with their potential interactions, as well as with their optimum levels. The choice of the titanium-precursor type is found to be the predominant factor affecting the efficiency of TiO<sub>2</sub> for hydrogen gas evolution. The interaction between precursor type and surfactant type is also statistically significant. The statistically optimized study identifies that combining F-108 amphiphilic block copolymers with titanium(III) chloride solution leads to TiO<sub>2</sub> exhibiting the highest photocatalytic efficiency for the generation of molecular hydrogen. The thus prepared TiO<sub>2</sub> shows relatively high photocatalytic hydrogen evolution rates ( $1.22 \text{ mmol h}^{-1} \text{ g}^{-1}$ ) compared to the commercially available TiO<sub>2</sub> photocatalysts which are not active for hydrogen generation in the absence of a co-catalyst. Significant photocatalytic reforming of ethanol is achieved over the synthesized bare TiO<sub>2</sub> with the formation of acetaldehyde as the main by-product in the gas phase. This unexpected photocatalytic performance is mainly attributed to the shift of flat band potential towards more negative potentials as revealed from the characterization results in addition to the high density of charge carriers exhibiting longer lifetime shown by laser transient reflectance measurements. The latter showed the presence of a high number of trapped states, which are beneficial for the photocatalytic properties.

## 1. Introduction

Clean energy systems are increasingly required to meet the growing global energy demand and to overcome the environmental problems of our modern society. Molecular hydrogen is considered to be one of the best fuels for the future. Hence, the photocatalytic generation of hydrogen using nanoparticle photocatalysts has attracted tremendous attention because of its potential production with reasonable cost as well as due to the involvement of green processes [1]. A photocatalytic reforming of organic compounds can simultaneously be performed during the generation of molecular hydrogen, which is considered as a considerable added value of this technique [2]. However, the lack of materials that could efficiently harvest the solar light is still the main obstacle hindering the transformation of this technique into practical

applications.

Although TiO<sub>2</sub> absorbs mainly in the UV region, it is widely used in various photocatalytic applications because of its high reactivity, non-toxicity, low cost, stability, and resistance to photocorrosion [2,3]. The first hydrogen gas generation through the photoelectrocatalytic splitting of water was reported by Fujishima and Honda in 1972 [2,4]. Since this time TiO<sub>2</sub> has been extensively studied in order to enhance its photo-response by harvesting of a wider range of the solar spectrum. Generally, a large surface area and high crystallinity are highly important parameters affecting the activity of the catalysts [5]. Mesoporous structure is one of the characteristics that gives good catalytic specifications to the materials, as it exhibits large surface area and pore-channels that ensure great mass diffusion within its frameworks [6]. In addition, loading noble metals and doping either with ions or with non-

\* Corresponding author at: Institut für Technische Chemie, Leibniz Universität Hannover, Callinstr. 3, D-30167 Hannover, Germany.

E-mail address: [alsalka@iftc.uni-hannover.de](mailto:alsalka@iftc.uni-hannover.de) (Y. AlSalka).

metals have been extensively explored to shift the light absorption of  $\text{TiO}_2$  towards the visible region and to lengthen the lifetime of the photogenerated charge carriers [7]. Recently, defective  $\text{TiO}_2$  has shown an enhanced visible-light absorption and improved photocatalytic performance, which has been attributed to oxygen vacancies and to the introduction of trapped states below the conduction band of the semiconductor [8].

Evaporation-induced self-assembly (EISA), was first reported by Ozin [9] and Brinker [10], and was considered as a one of the synthesis methods used to obtain thin films of mesoporous  $\text{TiO}_2$ . This soft-templating method is characterized by its simplicity, and efficiency [11]. It possesses several advantages compared to conventional sol-gel methods, e.g., performing the preparation under relatively mild conditions [12]. EISA process starts by dissolving block copolymer surfactant in suitable solvent followed by adding a calculated amount of titanium precursor(s) in acidic medium to form titania-surfactant hybrid phase. This phase contains terminal hydroxyl groups that interact through H-bonding with the hydrophilic portion of the block copolymer. An aging step takes place afterwards to get condensed titania network followed by calcination step to remove the surfactant. The main drawback of preparing  $\text{TiO}_2$  by EISA method is the uncontrolled hydrolysis and condensation of  $\text{Ti}^{4+}$  leading to the formation of poorly structured materials [11]. Adding coordinating agents, like acetylacetone, chelates Ti cations by forming metal complexes, thereby reduce the effects of a nucleophilic attack from water and lower hydrolysis kinetics [13]. Hydrolysis can also be controlled by employing a water-alcohol mixture instead of water only as a solvent, because alcohols possess relatively weaker nucleophilic behaviour [14]. Many studies have been conducted to discover the effect of EISA process parameters on the final product. Crepaldi et al. [15] tested the influence of six variables on the preparation of  $\text{TiO}_2$  films including the type of surfactant, the ratio of surfactant to precursor, the quantity of water in the reaction, the humidity, and the synthesis temperature. Among these variables, the humidity during synthesis had remarkable effect on the structure of the material. Soler-Illia and Sanchez [16] found that titanium butoxide (TBT), titanium isopropoxide (TTIP), and titanium ethoxide (TET) possessed different reaction activities toward water, hence different hydrolysis behaviours. Yang et al. [17] reported the production of mesoporous metal oxides, including  $\text{TiO}_2$ , by using metal chloride salts and P-123 surfactant. Luo et al. [18] obtained different phases of  $\text{TiO}_2$  by changing the surfactant and the solvent used with  $\text{TiCl}_4$  as a precursor. A mixture of anatase and rutile, in addition to pure rutile phase were synthesized by employing P-123 or F-127 as surfactants while varying the solvent (methanol, ethanol, 1-butanol and 1-octanol). By tuning the amount of  $\text{TiCl}_4$  in the presence of P-123, highly ordered mesoporous  $\text{TiO}_2$  photocatalysts were produced in mixed phase of anatase and rutile with different ratios [19]. Bosc et al. [20] synthesized mesoporous anatase  $\text{TiO}_2$  films using titanium(IV) isopropoxide and tri-block copolymers (Pluronic P-123, F-127). On the other hand, Masolo et al. [5] evaluated the effect of different titanium precursors, the calcination rate, and different ligands on the synthesized mesoporous  $\text{TiO}_2$  samples. These parameters influenced the morphology and the phase content of the final products. The ratio between rutile and anatase was related to the precursor's types and their proportions. They also found that acetylacetone resulting in a narrow pore size distribution, which played a major role in the photoactivity. The calcination rate had the less influence among the studied factors on both, the crystallinity and the mesoporosity of the material. On the other hand, removing the surfactant by thermal treatments was found to be a key step in EISA process. A calcination temperature below 400 °C is preferred to be used to remove most non-ionic triblock copolymers, because under higher temperatures the mesopore structures tend to collapse [21,22].

In spite of the successful studies conducted previously to prepare thin films of  $\text{TiO}_2$  [5], unfortunately, only few works are addressed to the synthesis of  $\text{TiO}_2$  powder through EISA method. Moreover in most

precedent works, several parameters affecting the EISA process have been changed while ignoring other factors or neglecting real optimization procedures. Conducting systematic studies defining the most important factors affecting EISA technique is also missing or not fully discussed. Furthermore, the use of limited types of titanium precursors, in particular the difficult handled precursor  $\text{TiCl}_4$ , is a common characteristic among most previous studies.

To find the optimum conditions, most experiments are usually performed by changing the levels of one factor at a time in an unsystematic way. However, this process suffers from lack of information concerning the optimum parameters once an interaction among the studied factors is carried out. This observation was confirmed by Fischer [23], who firstly introduced the principles of the Design of Experiments (DoE). DoE is a statistical tool used to conduct and to plan experiments in a methodological process allowing obtaining the maximum amount of information in the fewest number of runs. The design and analysis of experiments revolves around the understanding of the effects of different variables on other variable(s). The dependent variable is called the response, while the independent variables are called factors, and the experiments are run at different factor values, called levels. The total number of runs in DoE is equal to the number of levels "NL" powered to the number of factors "NF" (NLNF). DoE provides a strict mathematical framework by changing all pertinent factors simultaneously, in order to achieve the optimization using the fewest experimental runs [24]. When DoE is coupled with a full factorial design (FFD), multiple factors are investigated simultaneously during the test. It is possible additionally to optimize the significant factors affecting the process, determine the influence of these factors on specified responses, and specify the possible interactions between them [25].

Due to the time required to establish any normal optimization process, in addition to the high costs of consuming chemicals, we decided to benefit from the advantages of DoE to optimize the production of  $\text{TiO}_2$  via EISA method. Through the present work, DoE coupled with the analysis of variance (ANOVA) has been applied to discover, in a systematic statistical way, the effects of several factors on EISA method. The optimum values have been then identified through the same methodology and was applied to synthesis highly active  $\text{TiO}_2$  in powder form. The influence of both, the type of titanium precursor(s) and their proportions in addition to the type and quantity of surfactant are the main core of our investigations. The use of an easy-handled titanium precursor instead of  $\text{TiCl}_4$  is further discussed in details. The material synthesized based on the optimum parameters is then characterized and compared with the commercially available photocatalysts.

## 2. Experimental

### 2.1. Raw materials

All chemicals were used as received without any further purification. Titanium(IV) chloride ( $\geq 99.0\%$ ), titanium(IV) butoxide (97%), triblock copolymers pluronic F-108 and P-123, and acetylacetone ( $\geq 99\%$ ) were purchased from Sigma-Aldrich. Titanium(III) chloride 15% in HCl 10% was purchased from Merck. Methanol ( $\geq 99.9\%$ ) and ethanol ( $\geq 99.8\%$ ) were purchased from Carl-Roth. Deionized water was obtained from Millipore Mill-Q system at a resistivity of 18.2 MΩ cm at 25 °C.

### 2.2. Preparation method

The Evaporation-Induced Self-Assembly (EISA) method was employed to prepare  $\text{TiO}_2$  samples [26,27]. In a typical synthesis, 1 g of triblock copolymer surfactant (either F-108 or P-123) was dissolved in 20 ml of ethanol under vigorous stirring followed by the addition of 1 ml of acetylacetone. Then, the calculated amounts of titanium precursor(s) were added with continuous stirring at room temperature for

2 h. The mixture was then transferred to a petri dish and heat treated at 40°C for 24 h followed by calcination at 400°C for 12 h (at a heating rate of 4°C/min).

### 2.3. Statistical evaluation of significant factors using design of experiment (DoE)

DoE analysis was performed using Weibull ++/ALTA PRO software from Reliasoft. A general Full Factorial Design (FFD) of 16 runs was built to investigate the effects of three factors on the prepared materials: titanium-precursor type (PT), surfactant type (ST), and surfactant quantity (SQ). The photocatalytic evolution of hydrogen gas and the BET surface area were chosen as the responses to be monitored. Experimental runs were conducted in duplicate and in random order to reduce error. Generally, when all of the factors are quantitative, an alternative to replicating the combinations in the model is to apply a center point of the design and perform replicate runs at this center point. Such procedure can improve the precision of estimates for factorial effects and provides a check on linearity of the factor effects [28]. However, because two of the input factors, i.e. PT and ST, are qualitative factors, center point experiments are not implemented in the present study. The treatment of results was based then on the analysis of variance ANOVA using partial sum squares and 5% level of significance. Table 1 illustrates the FFD summary with all related variables.  $\text{TiCl}_4\text{:Ti(OBu)}_4$  in molar ration of (0.4:0.6) was firstly chosen as a precursor, to obtain  $\text{TiO}_2$  in pure anatase phase, as reported in literature [26].  $\text{TiCl}_4$  was then replaced by  $\text{TiCl}_3$  and mixed with  $\text{Ti(OBu)}_4$  while keeping the same used molar ratio between them. Two types of triblock copolymers "surfactants", i.e., P-123 (PEO19-PPO69-PEO19) and F-108 (PEO132-PPO50-PEO132) were chosen because of the difference in their blocks. P-123 with 69 PPO units has a significantly lower critical micelle concentration (cmc) and lower hydrophilic lipophilic balance value (HLB) than F-108 with 50 PPO units [29,30].

### 2.4. Characterization

The X-ray powder diffraction (XRD) measurements were performed on a Bruker DB Advance diffractometer (Bruker AXS GmbH) with a Bragg-Brentano geometry using  $\text{Cu K}\alpha$  radiation. The average crystallite sizes ( $D$ ) were calculated according to Scherrer's formula shown in Eq. 1, where  $K = 0.94$  is Scherrer constant,  $\lambda = 0.154 \text{ nm}$  is the x-ray wavelength of the  $\text{CuK}\alpha$ ,  $\beta$  is the full width of the peak measured at half maximum intensity, and  $\theta$  is the Bragg's angle of the peak.

$$D = \frac{K \cdot \lambda}{\beta \cdot \cos\theta} \quad (1)$$

The optical properties of powders were measured by recording the diffuse reflectance spectra in the range of 300–800 nm. Varian Cary 100 Bio UV/VIS spectrophotometer equipped with an integrating sphere diffusing reflectance accessory was used along with  $\text{BaSO}_4$  as a reference material. The measured reflectance data  $R$  were transformed to the Kubelka-Munk function  $f(R)$  [31] to determine the value of the band gap via the Tauc plot.

Flat-band potential  $E_b$  and the density of charge carriers (ND) were

**Table 1**  
Summary of full factorial design with 3 factors in 2 levels.

Fct.	Level 1	Level 2	Resp.1	Resp.2
PT <sup>a</sup>	$\text{TiCl}_4\text{:Ti(OBu)}_4$	$\text{TiCl}_3\text{:Ti(OBu)}_4$	$\text{H}_2$ rate	$S_{\text{BET}}$ <sup>d</sup>
ST <sup>b</sup>	F-108	P-123	$\mu\text{mol h}^{-1} \text{g}^{-1}$	$\text{m}^2 \text{g}^{-1}$
SQ <sup>c</sup>	1 g	2 g	$\mu\text{mol h}^{-1} \text{g}^{-1}$	$\text{m}^2 \text{g}^{-1}$

<sup>a</sup> Titanium-precursor type (PT).

<sup>b</sup> Surfactant type (ST).

<sup>c</sup> Surfactant quantity (SQ).

<sup>d</sup> BET surface area ( $S_{\text{BET}}$ ).

estimated by Mott-Schottky (M-S) relationship. Thin Titania films were deposited on FTO by the same EISA process utilized in this work. (M-S) measurements were conducted in a three-electrode electrochemical cell filled with  $\text{KCl}$  0.1 mol l<sup>-1</sup> at (pH 7) using IviumStat potentiostat at three different frequencies (1, 10 and 100 KHz).

Field-Emission Scanning Electron Microscopy (FE-SEM) and Energy-Dispersive X-ray Spectroscopy (EDX) measurements were carried out on a JEOL JSM-6700 F field emission instrument using a secondary electron detector (SE) at an accelerating voltage of 20 kV. High-Resolution Transmission Electron Microscopy (HR-TEM) measurements were performed using Tecnai G2 F20 TMP (FEI) with an acceleration voltage of 200 kV field emission gun (FEG).

BET surface area was measured by the single-point standard Micromeritics FlowSorb II 2300 instrument equipped with a Micromeritics AutoMate 23. Adsorption/desorption isotherms were recorded using the Autosorb-iQ automated gas sorption analyser (Quantachrome) equipped with ASiQwin data software.

### 2.5. Transient reflectance spectroscopy

Nanosecond diffuse reflectance laser flash photolysis spectroscopic measurements were performed as described by Schneider et al. [32], where the excitation of powder in a flat quartz cuvette was proceeded with a 6 ns UV-laser at 355 nm A pulsed xenon lamp (Osram XBO; 150 W) equipped with a cut-off filter (400 nm) is focused onto the samples and the reflected light was detected between 750 and 425 nm (in 25 nm steps) by Hamamatsu PMT R928 detector. Prior to the analysis, each powder sample was flushed with nitrogen gas for 30 min A terminal resistance of 50  $\Omega$  was used to facilitate a short rise time and fast observation of the signal after 40 ns, i.e., the period after which the signals related to the charge carrier were analyzed [33]. For easier processing and fitting of the transient signals, the optical reflectance changes  $\Delta J$  of the powder samples were calculated from the absorbance values as shown in Eq. 2, where  $I_0$  and  $I$  are the reflected lights before and after the laser excitation, respectively.

$$\Delta J = 1 - 10^{-Abs} = \frac{I_0 - I}{I_0} \quad (2)$$

### 2.6. Photocatalytic hydrogen gas evolution

The experiments of photocatalytic evolution of hydrogen gas were carried out in a batch photocatalytic system. All experiments were performed in 10 ml crimp glass vials tightly closed with crimp cap and silicon septum. In a typical experiment, 10 mg of the photocatalyst powder were suspended into 6 ml aqueous solution containing 4.28 mol l<sup>-1</sup> of hole-scavenger (typically ethanol). All the photocatalysts were introduced following the calcination procedure to insure the decomposition of any organic surfactant. In addition, a separate photocatalytic baseline experiment has been done, in which no surfactant was used during the synthesis procedure. After purging with pure argon (> 99.999%) for 15 min, the vials were horizontally fixed inside an orbital shaker placed at 30 cm distance below a 1000 W xenon lamp (Hönle UV Technology, Sol 1200) as a simulated solar light. From the measurement of the spectral irradiance in the wavelength range between 350 nm and 380 nm at the irradiated area, the photon flux was found to be  $I_0 = 383 \times 10^{-6} \text{ mol.m}^2 \text{s}^{-1}$ . Ignoring loses of light due to reflecting and scattering out,  $1.42 \times 10^{-7}$  mole of photons is entering the irradiated suspension per second.

The photocatalytically evolved molecular hydrogen was quantitatively determined by means of GC. For this purpose, a 50  $\mu\text{l}$  gas sample was periodically taken from the head space over the suspension using a Valco gas tight sampling syringe equipped with a push-button valve. The gas sample was then injected into the injection port of a Shimadzu GC-8 A, equipped with a TCD detector and a stainless-steel molecular sieve 5 A GC column (Sigma-Aldrich). The column temperature was

fixed at 80 °C, while the temperature of both, the injector and the TCD detector was maintained at 120 °C. The general relative standard deviation (RSD) of the set of data ranged between 4.8% and 6.5% depending on the sample, where each photocatalytic test was repeated in triplicate, each in a separate reaction vial.

Acetaldehyde was also analysed in gas phase over the reaction mixture by head-space/GC-MS technique using GCMS-QP5000 (Schimadzu) coupled with AOC-5000 Plus head-space autosampler. A capillary RTX-Wax column (30 m × 0.32 mm, dF = 0.25 μm; Restek) was used employing parameters applied by Cordell et al. [34]. High Performance Ion Chromatography (HPIC) was used to detect the products of ethanol conversion in liquid phase. HPIC analysis was performed using a Dionex ICS-1000 with a conductivity detector and an electro-regenerator suppressor. The eluent of  $9 \times 10^{-3}$  mol.l<sup>-1</sup> of sodium carbonate was pressed through an Ion pac As9-HC 2 × 50 mm column.

### 3. Results and discussion

#### 3.1. Statistical study of the factors affecting the synthesis of TiO<sub>2</sub>

As mentioned previously, DoE suggested a design of (2<sup>3</sup>) runs built automatically according to the studied factors. Conducting just 8 runs in duplicate, with a total of 16 runs, is found to be very convenient and quick to explore the effects of the studied factors. This feature in decreasing the number of experiments would undoubtedly reduce the errors and save time. Table 1S shows the values of both responses that introduced in FFD design, which are the BET surface area and the evolved hydrogen gas. Upon changing the levels of the employed factors, the BET surface area deviated over a very small range (106–123 m<sup>2</sup> g<sup>-1</sup>) in contrast to the photocatalytic evolution of hydrogen that underwent huge variations (425–999 μmol h<sup>-1</sup> g<sup>-1</sup>). These observations obviously confirm that the photocatalytic activities are significantly affected by changing the levels of the studied factors. Because the same changing in factors has much smaller effect on the BET surface area, it suggests that the correlation between the photocatalytic activity and the surface area is less than expected. However, the photocatalytic hydrogen gas evolution was approximately decreased to half when the surfactant had been excluded during the synthesis procedure. This could be related to the decreasing of the BET surface area.

The analysis of variance (ANOVA) is provided in Tables 2 and 2S. The goodness-of-fit statistics mentioned in these tables could be used to determine how well the model fits the data. Standard deviation values (S) of 17 and 0.7 indicate that the standard deviations between the experimental data points and the fitted values are approximately 17 μmol h<sup>-1</sup> g<sup>-1</sup> and 0.7 m<sup>2</sup> g<sup>-1</sup> for the hydrogen evolution and the BET surface area, respectively. However, such low S values by

**Table 2**

The factors and their interaction effects on the photocatalytic hydrogen evolution (ANOVA results) in FFD.

Source of Variation	D.F.	Sum of Squares	Mean Squares	F Ratio	P Value <sup>a</sup>
Model	7	6.20E+05	8.86E+04	3.05E+02	4.53E-09
PT	1	4.95E+05	4.95E+05	1.70E+03	1.30E-10
ST	1	1.15E+05	1.15E+05	3.94E+02	4.30E-08
SQ	1	6.03E+03	6.03E+03	2.08E+01	1.86E-03
PT • ST	1	3.96E+03	3.96E+03	1.36E+01	6.13E-03
PT • SQ	1	9.41E+01	9.41E+01	3.24E-01	5.85E-01
ST • SQ	1	4.10E+01	4.10E+01	1.41E-01	7.17E-01
PT • ST • SQ	1	5.40E+01	5.40E+01	1.86E-01	6.78E-01
Residual	8	2.32E+03	2.91E+02		
Pure Error	8	2.32E+03	2.91E+02		
Total	15	6.23E+05			

<sup>a</sup> α = 0.05, S = 17.04, R<sup>2</sup> = 99.63%, R<sup>2</sup>(adj) = 99.30%.

themselves do not indicate that the model meets the model assumptions. The coefficient of determination R<sup>2</sup> is a statistical measure of how close the data are to the fitted regression line. It could be used to determine how well the model fits the data, hence measure the goodness-of-fit. The calculated values of R<sup>2</sup> and adjusted R<sup>2</sup> are more than 98.8%, which means that both regression modes account for more than 98.8% of the variance. In general, the more variance that is accounted for by the regression model the closer the data points will fall to the fitted regression line. With such high values, the regression models show a very good variability and validity [35].

ANOVA results reveal that each of the studied three factors is statistically significant on both responses. This can be seen from a P value below the level of significance (α = 0.05). "PT" exhibits a P value of 1.3E-10, which is the lowest P value among the whole design of the hydrogen evolution response (see Table 2). Titanium-precursor type therefore possesses the highest statistical impact on this response. On the other hand, with its lowest value of P = 5.2E-10 (see Table 2S), the surfactant type "ST" is statistically the most intense factor affecting the BET surface area. However, because all the studied factors possess lower P values than the level of significance, all these factors affect statistically the both responses but in different magnitudes. The rank ordering of the statistically significant factors can also be discovered from the Pareto charts provided in Fig. 1.

Pareto chart can be used to determine the magnitude and the importance of the effects. This chart plots a reference line to indicate which effects are statistically significant. On the Pareto chart, bars that cross the reference line are statistically significant at the 0.05 level with the current model terms. Fig. 1 shows again that titanium-precursor

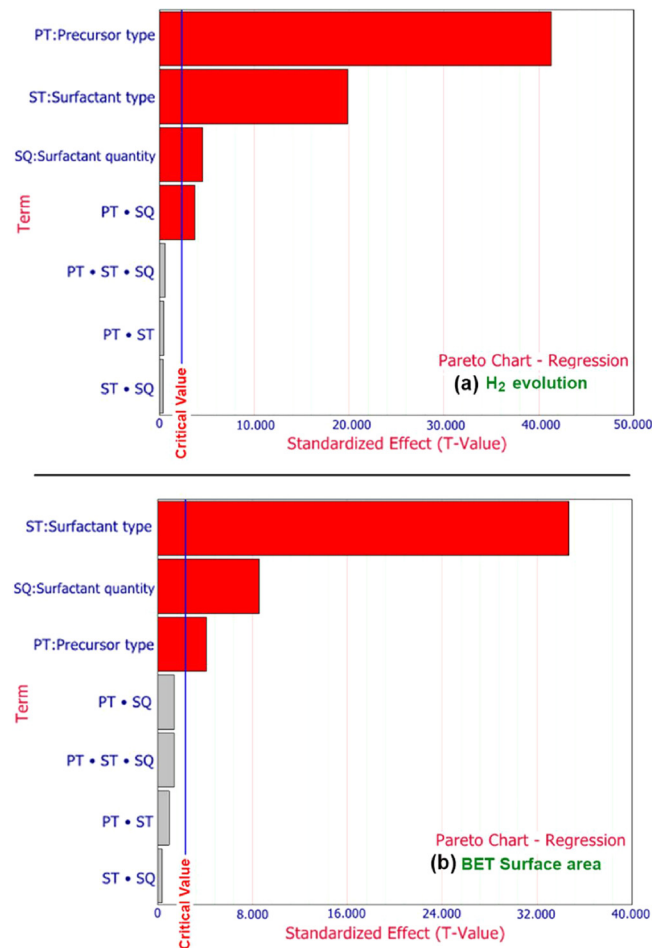


**Fig. 1.** Pareto Charts delivered from Full Factorial Design and ANOVA test for hydrogen evolution (a) and BET surface area (b).

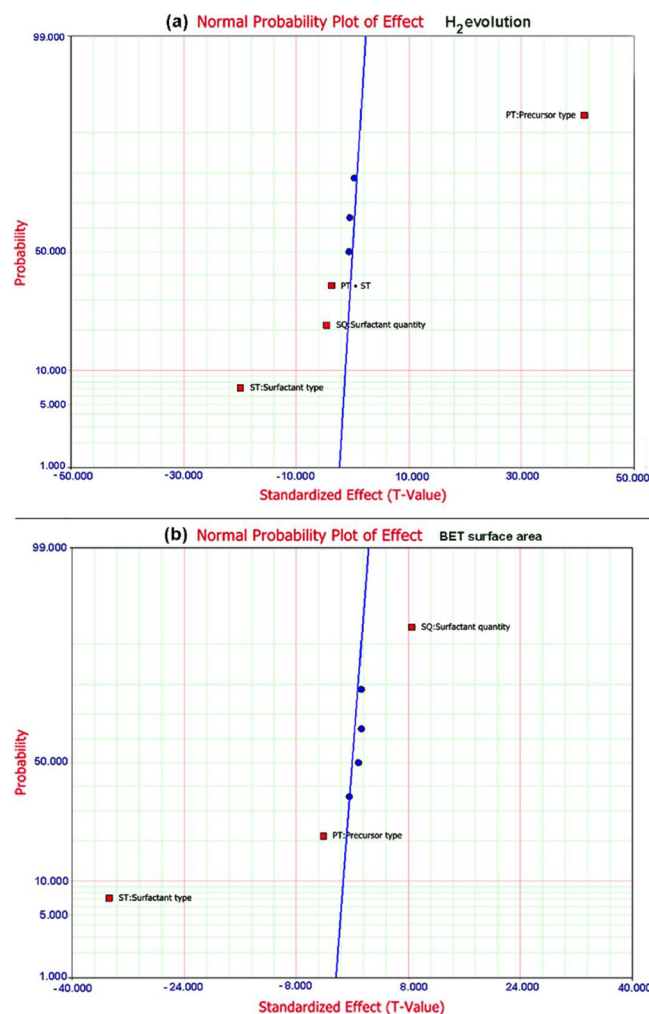


**Fig. 2.** The normal probability plots delivered from ANOVA analysis showing the magnitude, direction and the importance of the effects on the hydrogen evolution (a) and the BET surface area (b).

type (PT) is the predominant factor affecting the hydrogen evolution followed by the effect of surfactant type. On the other hand, the surfactant type (ST) is the predominant factor affecting the surface area followed by the effect of surfactant quantity. However with a T-value more than 40, PT shows the most intense impact among all the studied factors. Because the Pareto chart displays the absolute value of the effects, it is able to determine which effects are larger without determining which effects increase or decrease the response. The normal probability plot of the standardized effects can be therefore used to examine the magnitude, direction and the importance of the effects on one plot. In the plots presented in Fig. 2, effects that are further from 0 are statistically significant with greater magnitude. In the agreement with the previously mentioned conclusion, all the studied factors are statistically significant at the 0.05 level, since the colour and shape of the points differ between statistically significant (red squares), and statistically insignificant effects (blue circles). In addition, positive standardized effects increase the response when the settings change from the low value of the factor to the high value. In case of the hydrogen evolution response, the precursor type has a positive standardized effect (see Fig. 2(a)). Hence, the high level of this factor, which is  $\text{TiCl}_3$ -based precursor, increases the hydrogen evolution. Surfactant type and surfactant quantity have in contrast negative standardized effects. Consequently using the low levels of these factors, which are F-108 and 1 g, increases the hydrogen evolution as well. Similarly, the BET surface area increases (see Fig. 2(b)) when  $\text{TiCl}_3$ -based precursor

and F-108 were used, as they are the low values of each factor (negative standardized effects). The standard deviation for BET measurement is determined to be  $SD = 0.61$  for the sample synthesized using  $(\text{TiCl}_3:\text{TiBu}(\text{OH})_4)$  and 1 g of F-108, with a corresponding coefficient of variation of  $COV = 0.52\%$ . On the other hand, the coefficient of variation of all the 16 BET measurements is calculated to be  $COV = 5.69\%$ .

The interaction of the studied factors shown in Pareto chart and in the interaction matrix plots (see Fig. 3) was statistically insignificant in term of BET surface area, which means that the deference in precursor type is independent from the surfactant type or its quantity and vice versa. On the other hand, the interaction between precursor type and surfactant type was the only statistically significant interaction affected the photocatalytic hydrogen evolution as observed from its P value. The interaction plots could be used to show how the relationship between one factor (e.g. PT) and a response (e.g.  $H_2$  evolution) depends on the value of a second factor (e.g. ST). It plots the means for each level of a factor while the level of a second factor held constant. Interaction is present when the lines are not parallel to each other. This could be slightly noticed in the case of the interaction between PT and ST shown in Fig. 3. A plot of the response ( $H_2$  evolution) of precursor type "PT" at different levels of surfactant type "ST" shows that the response is changed with the levels of PT, but the effect of PT on the response could also depend on the level of ST.

In this instance, the photocatalytic hydrogen evolution is always higher when using  $\text{TiCl}_3$ -based precursor rather than  $\text{TiCl}_4$ -based precursor for  $\text{TiO}_2$  synthesis as clearly shown in the term effect plot presented in Fig. 4(a). When the line of the term-effect plot is not horizontal, different levels of the factor affect the response differently. The Fig. 4(a) indicates a higher evolution of hydrogen gas when F-108 rather than F-127 is used as a templating surfactant. On the other hand, the photocatalysts synthesized employing F-108 shows the highest BET surface area values, which could be related to the higher ratio of the hydrophobic PEO block resulting in higher numbers of smaller hydrophobic cores in the surfactant micelles [36]. Interestingly, while the surface area was slightly increased by increasing the amount of surfactant, the molecular hydrogen evolution was slightly decreased. However, the less horizontal the line in the term-effect plot, the greater the likelihood that the effect is statistically significant. Therefore, the effect of surfactant amount could be considered as relatively negligible; consequently, the use of less amount of surfactant will result in same activity but lower costs.

Considering the previous statistical study, and based on the ANOVA outcomes, the optimization features of DoE were successfully utilized to identify the statistical optimization of factors. Fig. 4(b) presents the computed optimized conditions towards maximizing the photocatalytic hydrogen gas evolution. According to this figure, using  $\text{TiCl}_3$  based-precursor is preferable over  $\text{TiCl}_4$ . To conclude this part, the optimal solution that is used for the next optimizing step contains:  $\text{TiCl}_3:\text{Ti(OBu)}_4$  as a precursor and 1 g of F-108 as a surfactant.

### 3.2. Optimizing the ratio between $\text{TiCl}_3$ and $\text{Ti(OBu)}_4$

Since  $\text{TiCl}_3$ -based precursor was the crucial factor positively affecting the hydrogen evolution as shown previously, the molar ratio between  $\text{TiCl}_3$  and  $\text{Ti(OBu)}_4$  was further optimized to reach the highest rate of hydrogen. This optimization was excluded from the previous DoE study, because changing the molar ratio could affect several variables such as  $\text{TiO}_2$  phases, the optical absorbance and the crystalline size [26]. These changes could affect in turn the photocatalytic activity; therefore the responses could not be directly related to the studied factor. The experiments with different molar ratios of  $\text{TiCl}_3/\text{Ti(OBu)}_4$  were conducted, while fixing the total amount of titanium to  $(11.4 \times 10^{-3}$  mol) and utilizing 1 g of F-108 as a surfactant.

Table 3 shows photocatalytic activities of the thus obtained samples compared to the commercial photocatalyst UV100 and P25 photocatalysts. Interestingly, all the self-prepared materials were able to

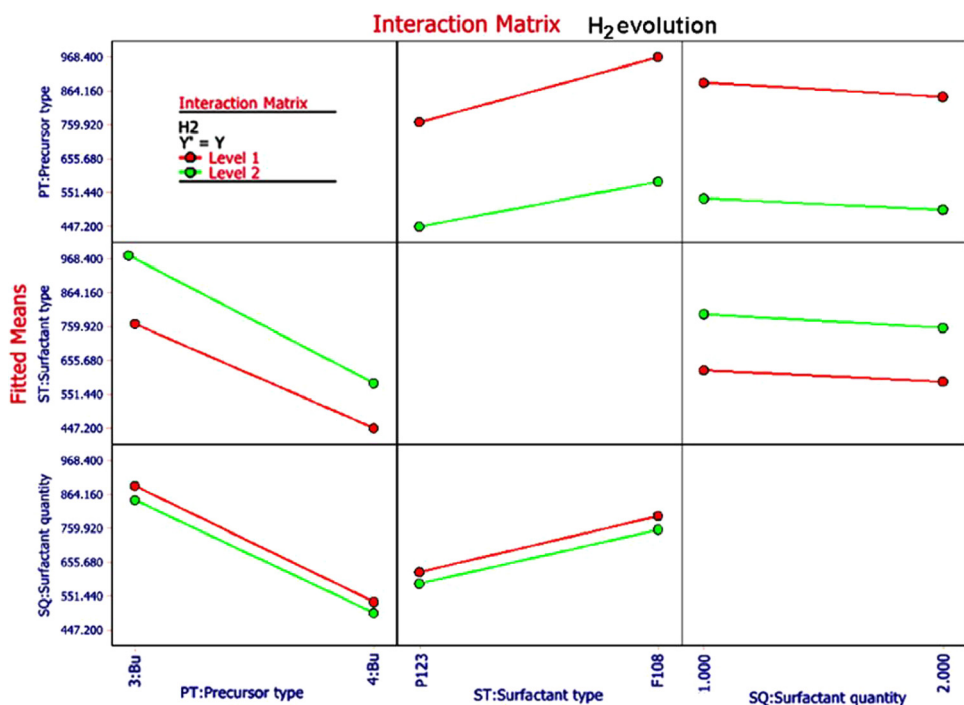


Fig. 3. The interaction matrix delivered from ANOVA analysis related to the hydrogen evolution response.

generate molecular hydrogen from ethanolic-aqueous solutions even in the absence of any co-catalyst. Table 3 highlights the strong dependence of the photocatalytic evolution of hydrogen on the quantity of  $\text{TiCl}_3$  in the precursor. The photonic efficiencies ( $\xi$ ) for the hydrogen evolution reaction have been calculated according to Eqs. 3 and 4 [37], and the results are presented in Table 3.

$$\xi (\%) = \frac{\text{formation rate} (\text{mol. s}^{-1})}{\text{photon flux} (\text{mol. m}^2. \text{s}^{-1})} \times 100 = \frac{V. \Delta c}{I_0. A. \Delta t} \times 100 \quad (3)$$

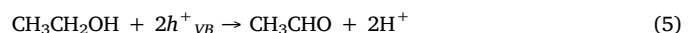
$$I_0 = \frac{I. \lambda}{N_A. h. c} \quad (4)$$

where  $V$  is the suspension volume ( $0.006 \text{ l}$ ),  $\Delta c/\Delta t$  is the formation rate ( $\text{mol.s}^{-1}$ ),  $A$  is the illuminated area ( $4.2 \times 10^{-4} \text{ m}^2$ ),  $I$  is the light intensity ( $\text{W.m}^{-2}$ ),  $\lambda$  is the corresponding wavelength ( $\text{m}$ ),  $N_A$  is the Avogadro's constant ( $6.02 \times 10^{23} \text{ mol}^{-1}$ ),  $h$  is the Planck constant ( $6.63 \times 10^{-34} \text{ W.s}^2$ ) and  $c$  is the velocity of light ( $3 \times 10^8 \text{ m s}^{-1}$ ). According to the results presented in Table 3,  $\text{TiCl}_3$  as a single precursor provides positive advantages for EISA method to synthesize active  $\text{TiO}_2$  material in powder form.  $\text{TiCl}_3$  seems to be the ideal precursor among the other tested precursors as it is easily handled solution that leads to the formation of bare  $\text{TiO}_2$  with approximately 1.5-fold higher photonic efficiency in comparison to other prepared materials. The use of  $\text{TiCl}_3$  as a precursor provides as well the simplicity and the reliability to EISA method, because it eliminates employing of alkoxides, which could negatively affect the final product.

### 3.3. The photocatalytic application over the optimized (S5) material

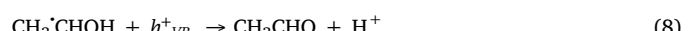
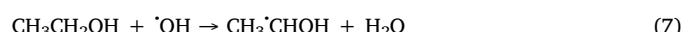
The photocatalytic activity was followed-up by the determination of molecular hydrogen and acetaldehyde formed in the gas phase in addition to the carboxylic acids formed in the liquid phase. The data were collected after two hours of irradiating an ethanolic aqueous suspension. Table 4 illustrates the huge differences in photocatalytic activities between the optimized photocatalyst (S5) and the UV100. Molecular hydrogen is only detected over S5, which is possessing much higher photocatalytic activity towards the conversion of ethanol. According to the literature, the surface defects serve additionally as adsorption sites

to transfer the charge carriers to the adsorbed species, thus promoting the photocatalytic reaction [38,39]. Around 7.1 mmol of ethanol (28% of the initial concentration) were decreased over S5 compared to 5.9 mmol (23.3%) over UV100. It is worth to mention that these values include both, the amount converted of ethanol as well as the amount adsorbed on  $\text{TiO}_2$ . This indicates the higher photocatalytic activity of the prepared material, because it exhibits around 2.4-fold lower surface area than UV100. The conversion of ethanol was accompanied with the formation of acetaldehyde and molecular hydrogen following the Eqs. 5 and 6, respectively [40] (Table 5).



Where  $\text{h}^+_{VB}$  and  $e^-_{CB}$  represent the holes and electrons, respectively, generated on the photocatalysts by light absorption.

It is well known that hydroxyl radicals ( $\cdot\text{OH}$ ) can react with ethanol, mainly through the abstraction of a hydrogen atom from the C–H bond (Eq. 7). This step is followed by the formation of acetaldehyde (Eq. 8) that is the principal stable product through the electron injection into the conduction band of  $\text{TiO}_2$ , a process called “current doubling” [41]. Current doubling mechanism occurs when using any alcohol carrying a hydrogen atom at the carbon atom in the  $\alpha$ -position to its hydroxyl group [42]. Ethanol was transferred over S5 to produce 0.43 mmol of acetaldehyde as the major by-product after 2 h of illumination. The quantity of acetaldehyde was 10-folds higher over S5 than in case of UV100. Simultaneously, 0.023 mmol of molecular hydrogen and traces of acetic acid (Eq. 9) were formed over S5 compared to undetectable amounts of these products over UV100.



Using the Eqs. (3) and (4), the photonic efficiencies of the formed products were calculated and listed in Table 4. The superior band structure of S5 has definitely positive impact. This includes the more negative potential of its flat band edge besides the higher charge carrier

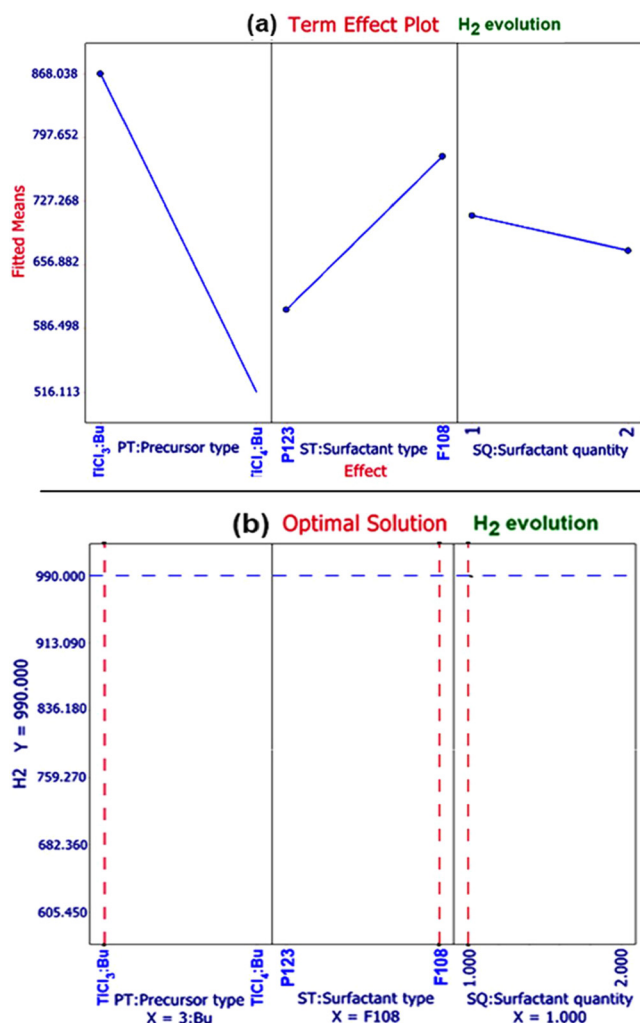


**Fig. 4.** the term effect plot for the hydrogen evolution based on the statistical tests (a), and the optimal solution towards maximizing hydrogen based on ANOVA result.

**Table 3**

Synthesis parameters with the photocatalytic activities of the different self-prepared materials in comparison with the commercially available photocatalysts.

#	TiCl <sub>3</sub> :Ti(OBu) <sub>4</sub>	H <sub>2</sub> μmol.h <sup>-1</sup> .g <sup>-1</sup>	ξ <sup>a</sup> %
S1	0.2:0.8	796.8 ± 38.1	1.5
S2	0.4:0.6	953.4 ± 46.8	1.9
S3	0.6:0.4	574.2 ± 37.2	1.1
S4	0.8:0.2	669.9 ± 40.4	1.3
S5	1:0	1221.6 ± 58.1	2.4
UV100		ND <sup>b</sup>	—
P25		ND <sup>b</sup>	—

<sup>a</sup> Photonic efficiency (ξ) calculated for the mean H<sub>2</sub> rate.

<sup>b</sup> Not detected (ND) after 2 h of illumination according to the limits of detection (0.4 μmol for H<sub>2</sub>) of the GC analysis.

density. The improvement of TiO<sub>2</sub> conductivity enhances the charge carrier transport from the bulk to the surface and the charge-transfer reaction [43]. Furthermore, the broad distribution of trapped states at different energetic depths, besides the better separation between the charge carriers could be the main reasons for such higher photocatalytic activity. Although the conversion of ethanol to acetaldehyde and molecular hydrogen was more efficient over our sample (S5), however, the amount of molecular hydrogen evolved over S5 was 18-folds lower than

the amount formed of acetaldehyde.

In order to investigate in more details the enhancement in the photocatalytic activity over the S5 sample, long-term experiments were conducted either under the full solar spectrum or in the presence of cut-off filter  $\geq 420$  nm. Using the same photocatalytic system, the hydrogen evolution was followed-up in 60 min intervals. S5 showed again much better photocatalytic activity even under visible light conditions. Fig. 5 illustrates the photocatalytic behaviour of S5 against the time. Molecular hydrogen was produced during the first 60 min under simulated solar irradiation and possessed linear increasing until 360 min, then the evolution followed a second linear increasing but in a lower rate. However the evolution of hydrogen was detected after 120 min under visible light and reached 10-fold lower amount at the end of the 600 min irradiation comparing the full solar light experiment. Several conversion products have been previously reported upon the photo-reforming of ethanol over Au/TiO<sub>2</sub> including acetaldehyde, acetic acid, acetone, ethene, ethylene and methane [40,44,45]. Our GC-MS analysis detected traces of methane, ethylene and carbon monoxide in gas phase; hence, the formation of such compounds could negatively affect the evolution of molecular hydrogen, as some of them are undesirable and or could not involve in the current doubling effect. UV100 on the other hand showed inactivity during the first 460 min before the evolution of relatively neglected amount of hydrogen gas over the rest period.

These results from the photocatalytic experiments suggested that detailed structural and optical characterizations for the prepared samples are needed.

#### 3.4. Physical and chemical characterisation of the synthesised materials

XRD measurements along with standard pattern of both, pure anatase (Natl. Bur. Stand. # 00-021-1272) and pure rutile (Natl. Bur. Stand. # 00-021-1276) are demonstrated in Fig. 6. By comparing the XRD patterns of pure anatase and rutile to those of samples synthesized using TiCl<sub>3</sub> with mole fractions of 0.6 and 0.8, one can clearly see the formation of mixed phases with different ratios of anatase and rutile. All the other samples exhibit only XRD pattern of a pure anatase. Data in Table 3 clearly confirm the crucial role of the crystalline phase, since materials having a pure anatase phase exhibited better photocatalytic activities. The photocatalytic hydrogen evolution was dramatically dropped down in the mixed-phase samples. This correlates with other reported results showing a higher hydrogen production for anatase-based TiO<sub>2</sub> photocatalysts due to the more negative potential of the conduction band edge and the presence of trapped states lying below its Fermi level [46]. On the other hand, many other researchers found a huge benefit of mixed-phase TiO<sub>2</sub> due to the synergistic effect of anatase and rutile [47,48].

SEM images presented in Fig. 1S for the material prepared from (100% TiCl<sub>3</sub>) show nanocrystalline spherical morphology for aggregated nano-sized particles with diameter of about 500 nm and a wide distribution of non-ordered pores throughout the aggregated particles. On the other hand, a grain size ranging from 9 to 12 nm for nanoscale powder with many crystal lattice planes and a good crystallinity is estimated from TEM and high-resolution TEM images presented in Fig. 2S (a) and (b), respectively. An apparent correlation between the hydrogen evolution and the surface area is clearly noticed among the prepared materials as illustrated in Fig. 7. The increase in the surface area from 105 to 121 m<sup>2</sup> g<sup>-1</sup> leads to 2.5-fold enhancement of the molecular hydrogen evolution rate. In contrast, the high surface area in case of UV100 does not reflect any activity towards the photocatalytic hydrogen evolution. These observations therefore point out to the dominant role of precursor type on the photocatalytic activity.

Fig. 3S (a) demonstrates the N<sub>2</sub> adsorption-desorption isotherms recorded for the nanostructured S5 photocatalyst. According to BET method, these isotherms revealed a type IV characteristic of mesoporous materials [49]. This result is in good agreement with

**Table 4**

Comparison between the photocatalytic activities of S5 and UV100 after 120 min of irradiation under simulated solar light.

#	Ethanol mmol	Acetaldehyde mmol	$\xi$ acetaldehyde %	Acetic acid mmol	$\xi$ acetic acid %	H <sub>2</sub> mmol	$\xi$ H <sub>2</sub> %
Initial	25.32	—	—	—	—	—	—
Photolysis	25.09	ND <sup>a</sup>	NA <sup>b</sup>	ND <sup>a</sup>	NA <sup>b</sup>	ND <sup>a</sup>	NA <sup>b</sup>
UV100	19.40	0.04.2	4.10	ND <sup>a</sup>	NA <sup>b</sup>	ND <sup>a</sup>	NA <sup>b</sup>
S5	18.24	0.430	42.1	$4.9 \times 10^{-6}$	$4.8 \times 10^{-4}$	0.023	2.20

<sup>a</sup> Not detected (ND).

<sup>b</sup> Not applicable (NA).

**Table 5**

Synthesis parameters with the physiochemical and optical properties of the different self-prepared materials.

#	TiCl <sub>3</sub> : Ti(OBu) <sub>4</sub>	S <sub>BET</sub> <sup>a</sup> m <sup>2</sup> g <sup>-1</sup>	A:R <sup>b</sup> %	D <sup>c</sup> (anatase) nm	E <sub>g</sub> <sup>d</sup> eV
S1	0.2:0.8	$116.1 \pm 0.9$	100	9.6	3.10
S2	0.4:0.6	$117.7 \pm 0.6$	100	11.4	3.08
S3	0.6:0.4	$104.7 \pm 0.6$	78	13.6	2.97
S4	0.8:0.2	$107.3 \pm 0.7$	86	13.2	2.98
S5	1:0	$121.3 \pm 0.9$	100	9.1	2.99
UV100		$289.5 \pm 1.4$	100	7.4	3.20
P25		$49.1 \pm 0.4$	72	21.5	3.05

<sup>a</sup> BET surface area (S<sub>BET</sub>).

<sup>b</sup> Anatase to rutile ratio (A:R) according to XRD measurements.

<sup>c</sup> Crystalline size (D) calculated from the XRD data.

<sup>d</sup> Energy band gap (E<sub>g</sub>) calculated from UV-VIS data and the Tauc plots.

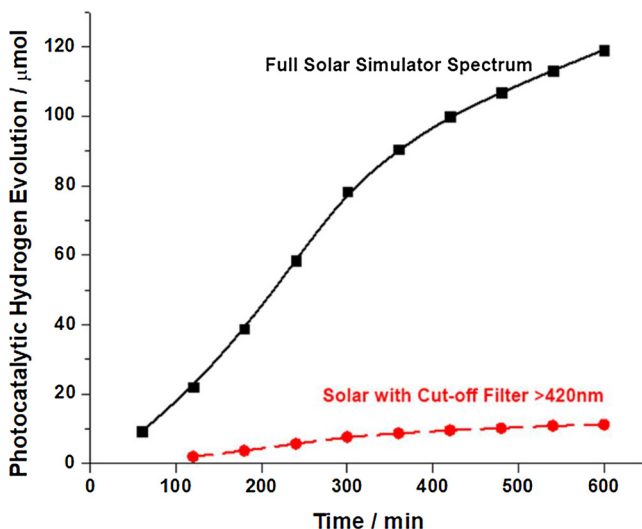


Fig. 5. long-term photocatalytic hydrogen evolution from ethanoic solution over S5 under full solar spectrum, and in the presence of cut-off filter of 420 nm.

predictions, as EISA soft-templating method is reported to increase the surface area through mesoporous structures [50]. The distribution of pore size shown in Fig. 3S (b) is calculated by BJH method, where the average pore diameter for S5 was 5.1 nm. Although the structure contained mesopores with a pore diameter range between 2 and 8 nm, however, these pores characterized as non-ordered and showed a wide distribution range. In Soft-templating methods including EISA, the mesostructures could collapse upon removing the surfactant by calcinations [51] leading sometimes to non-ordered mesopore structures. This is a drawback of soft-templating technique.

The optical properties of the prepared materials were measured by means of UV-VIS spectroscopy and the obtained reflectance data are presented in Fig. 8(a and b). A clear optical response in the visible range until around 600 nm can be noticed in TiCl<sub>3</sub>-based materials compared

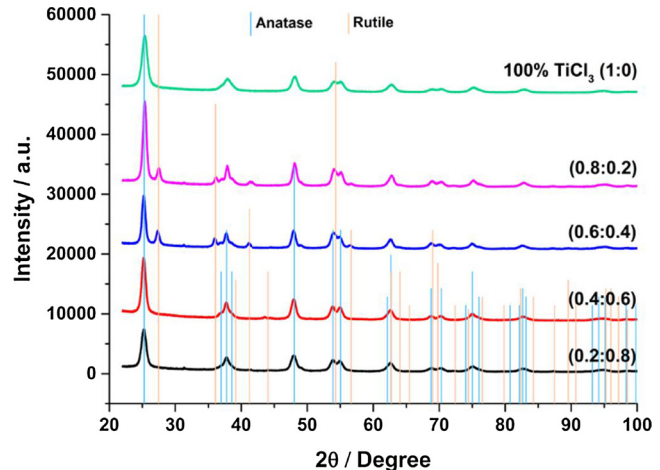


Fig. 6. XRD patterns of the self-prepared photocatalysts compared to the standard patterns of anatase and rutile.

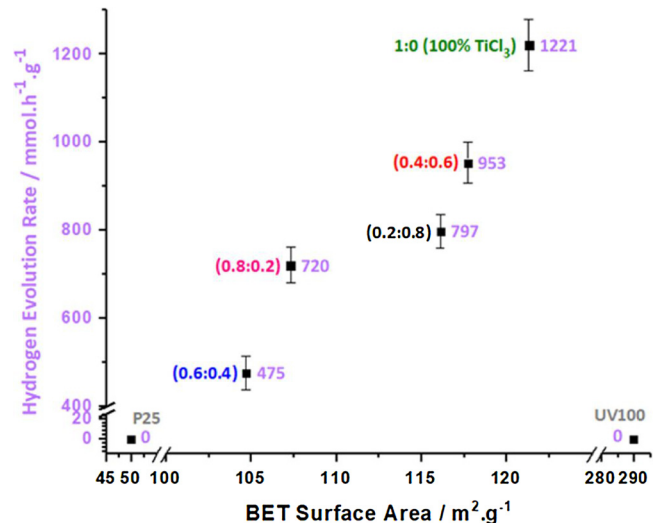


Fig. 7. relationship between the photocatalytic activity (after 120 min irradiation) and BET surface area for the self-prepared photocatalysts.

to UV100 that mainly absorb in UV range. This visible response is not due to doping with foreign atoms since the EDX analysis of all the self-prepared nanoparticles showed peaks for titanium and oxygen elements without any trace of other impurities within the detection limit of the EDX. Such visible light response was noticed by other researchers and has been attributed to defects in TiO<sub>2</sub> [8,48]. The energy band gaps were also affected throughout the prepared materials. A clear relationship between the quantity of TiCl<sub>3</sub> in the precursor and the band gap energies of the anatase samples is proven, since a narrowing of the band gaps upon increasing TiCl<sub>3</sub> ratio was noticed as demonstrated in Fig. 7(b) and Table 3. Because doping is unlikely to be happened as

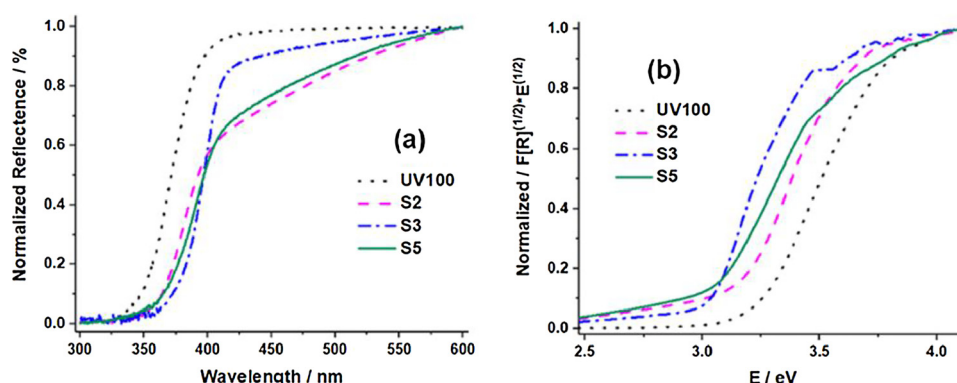


Fig. 8. UV-vis light reflectance spectra (a), and Tauc plots (b) of the tested photocatalysts.

stated before, the presence of defect states has been reported to drastically alter the electronic structure of the semiconductor. Such defects introduce additional energy levels in the middle of the band gap and could therefore narrow its band gap energy and improves the visible light absorption [52]. Oxygen vacancies represent the most common defects in  $\text{TiO}_2$ , which have been related to the unpaired electrons that were located initially in an O 2p orbital of the valence band. These electrons can then be transferred, by the removal of the corresponding oxygen atom, into the conduction band to interact with  $\text{Ti}^{4+}$  giving the corresponding  $\text{Ti}^{3+}$  defects, creating shallow and deep sub-band gap  $\text{Ti}^{3+}$  states below the conduction band [53–55].

The flat-band potentials were derived from the Mott–Schottky plots for electrodes of  $\text{TiO}_2$  thin film on FTO. The flat-band potential for the film prepared from  $\text{TiCl}_3$  through the same EISA method possessed a value of (-0.24 V vs. NHE at pH = 0). This result clearly proves that the narrowing in the band gap energy is accompanied with a shifting of the flat-band potential towards more negative potential compared to the  $E_{fb}$  for pure anatase  $\text{TiO}_2$  (-0.19 V vs. NHE) [56,57] and the  $E_{fb}$  for a self-prepared electrode prepared from  $\text{TiCl}_4$  in the same conditions (-0.17 V vs. NHE). The more negative the potential of the flat band is, the higher the reduction potential of the photogenerated electrons is. This leads to more favourable reduction reaction of  $\text{H}^+$  to produce molecular hydrogen ( $\text{H}^+/\text{H}_2 = 0 \text{ V}$  vs. NHE). Consequently, the valence band edges were calculated from the values of the band-gap energy and the flat-band potential. S5 material underwent a corresponding widening in its valence band edge to a less positive potential (2.74 V vs. NHE at pH = 0) comparing to both, the pure anatase  $\text{TiO}_2$  (3.00 V vs. NHE) and the electrode prepared from  $\text{TiCl}_4$  (2.98 V vs. NHE). Such effect was noticed by Wang et al. [58] who produced highly defective  $\text{TiO}_2$  with a widening in the valence band top edge leading to remarkably a higher photocatalytic activity compared with normal  $\text{TiO}_2$ . They explained this observation by the efficient charge transfer in bulk and at semiconductor/electrolyte interface. The shifting of the flat-band potential, together with the widening of the valence band edge point out once more to the presence of defects in the structure of  $\text{TiO}_2$ , especially, due to the absence of foreign dopants. The introduction of such defects has been usually accompanied with an increasing in the charge carrier densities (ND) of the studied materials. A charge carrier density value of  $9.3 \times 10^{20} \text{ cm}^{-3}$  in S5 sample was recorded upon the analysis of its M-S plots. This value is noticeably higher than that of pure anatase  $\text{TiO}_2$  ( $0.4\text{--}0.8 \times 10^{19} \text{ cm}^{-3}$ ) [56] and of the electrode prepared from  $\text{TiCl}_4$  ( $8.1 \times 10^{19}$ ). The density of the charge carriers affects the depletion layer and the recombination rate of the semiconductor [59]. Kang et al. [60] noticed a negative shift of  $E_{fb}$  upon  $\text{NaBH}_4$  reduction due to the formation of defects, which serve as electron donors [13]. In addition, they found that  $\text{NaBH}_4$  treatment increases the donor density of reduced  $\text{TiO}_2$ , thus resulting in a higher electrical conductivity as well as in the faster charge carriers transport. Higher donor densities are expected to shift the Fermi level of  $\text{TiO}_2$  toward the conduction

band and to facilitate the charge separation at the semiconductor–electrolyte interface, by increasing the degree of band bending [13]. The same observations were reported by Mehta et al. [61], who found that treating  $\text{TiO}_2$  with hydrogen under partial pressure conditions enhanced the photocatalytic response due to surface defects, which induced a higher charge carrier concentration and a more negative flat band potential.

The 1.5-fold higher photonic efficiency of S5 in comparison to other prepared materials can be explained therefore by its higher optical absorption, as well as by the improved charge carrier creation and utilisation. Therefore, the synthesis of  $\text{TiO}_2$  starting from  $\text{TiCl}_3$  (sample S5) not only provides the simplicity of the synthesis method, but it enhances additionally the optical and the electronic properties of  $\text{TiO}_2$ , leading to increase both, the photocatalytic hydrogen evolution and the photonic efficiency, even in the absence of any co-catalyst.

### 3.5. Transient reflectance spectroscopy

The transient absorption spectra obtained for UV100 and S5 0.1  $\mu\text{s}$  after the laser pulse are presented in Fig. 9(a). While the powders being kept under an inert nitrogen atmosphere, the two materials showed broad spectra, which is in good agreement with the literature as the trapped charge carrier species absorb light over a broad wavelengths range [33]. It has been reported that the transient absorption signals observed for  $\text{TiO}_2$  above 600 nm are attributed to trapped electrons [62], whereas the transient absorption observed between 400 nm and 530 nm is attributed to the trapped holes [62,63]. Because the experiments were performed in the absence of any electron donor or acceptor the transient reflectance signals represent a sum of trapped electron and trapped hole states. Both measurements were identically repeated in  $\text{N}_2$ –methanol vapour environment to follow-up the changes in the transient absorption spectra and to link the transient signals to the possible trapped charge carriers. After the introduction of the methanol vapour no changes of the transient absorption signals has been observed for UV100 in the wavelength range from 650 to 710 nm, while the transient absorption intensity in the wavelengths range from 410 to 625 nm deteriorate (see Fig. 8a). Accordingly, the latter wavelengths range can be attributed to trapped holes reacting rapidly with methanol within 1 ns [64].

On the other hand, the transient absorption spectrum of S5 exhibits maximum at 650 nm that can be correlated to the d-d transition of the  $\text{Ti}^{3+}$  blue centres. However, the whole transient absorption spectrum in methanol environment has remarkably lower absorptions comparing to the  $\text{N}_2$  atmosphere. This clearly indicates the very broad distribution of trapped holes over the whole studied spectral range of wavelengths, which indicates that the holes are delocalized over different trapping sites, with the holes being trapped at different energetic depths resulting in such broad transient absorption spectra. Bahnemann et al. [65] confirmed that at least two different types of holes have to be

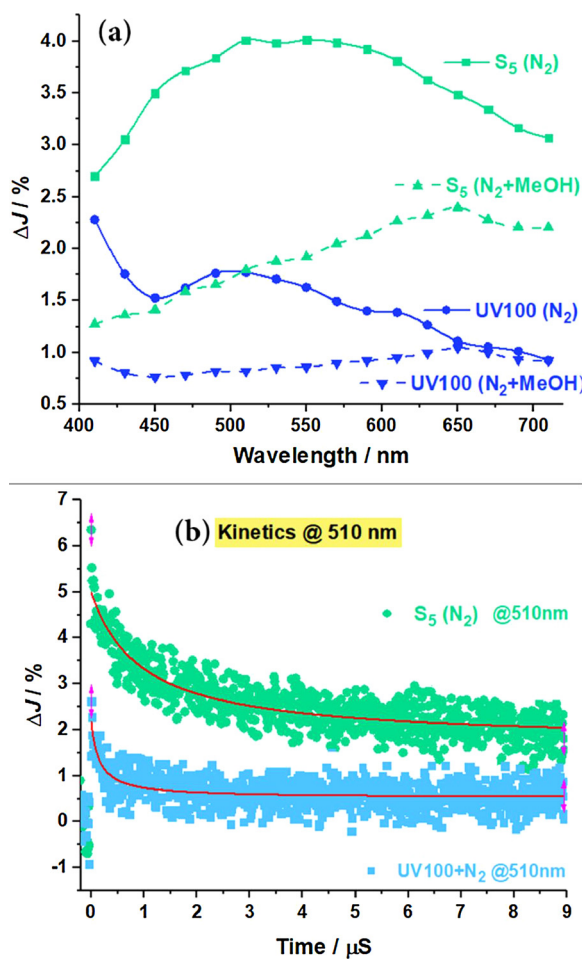


**Fig. 9.** Transient absorption spectra (a) measured at 0.1  $\mu$ s after laser excitation in a N<sub>2</sub> and a N<sub>2</sub>-methanol vapour atmosphere, transient absorption signals (b) observed at 510 nm in a N<sub>2</sub> and N<sub>2</sub>-methanol vapour atmosphere.  $\lambda_{\text{ex}} = 355$  nm with cut-off filter of 400 nm for detection.

considered, namely, the deeply poor-reactive trapped holes (at 450 nm) besides the free holes that possess a higher oxidation potential. It is well reported that the valence band holes can be rapidly transported to the surface, where a surface hole trap sites are formed on Ti-O<sub>s</sub>H and/or Ti-O<sub>s</sub>-Ti. These surface trapped holes (Ti-O<sub>s</sub>H<sup>+</sup> and/or Ti-O<sub>s</sub><sup>+</sup>-Ti) are the main oxidants for any adsorbed electron donor. The different trapped states for holes in addition to the higher reactivity with methanol in our self-prepared material point out the better migration of the charge carriers, as methanol can only react with the surface trapped holes, while the bulk carriers remain in the system [32]. The investigations delivered from the transient reflectance spectroscopy revealed a delocalization of holes over different surface trapping sites with a higher oxidation potential than other deeply trapped sites. Kong et al. [39] found that increasing the ratio of the concentration of surface defects to bulk defects improves the separation between the photogenerated carriers, thereby enhancing the photocatalytic activity. This conclusion has also been proposed by Ohtani [66], who claimed the necessity to control precisely the structural properties to develop high active photocatalysts. In this context, the density of surface shallow traps should be maximized and the density of deep traps minimized. It has been reported that defects in TiO<sub>2</sub> could perform as a co-catalyst, which enhance the usage of the photogenerated electrons in the reduction process [52]. Hole trapping sites participate in such surface defects that play a decisive role in adsorption and surface reactivity. They can serve as charge carrier traps as well as adsorption sites where the charge carrier transfer to adsorbed species can reduce the charge carrier

recombination [39].

The transient absorption kinetics for both materials at 510 nm in nitrogen atmosphere are presented in Fig. 9(b). Both signals showed an increase in absorption immediately after the laser pulse, however the self-prepared photocatalyst exhibited around 3-fold higher signal intensity of the initial absorption  $J_0$ . This result confirms the higher charge densities of the prepared material. A rapid decrease in the absorption signal is occurred followed by reaching a long-lasting, nearly constant absorption. The characteristic times after which  $J_0$  at 510 nm decays to  $J_0/e$  ( $\sim 37\%$ ) are around 0.5  $\mu$ s and 4  $\mu$ s for UV100 and S5, respectively. Comparing the transient absorption kinetics at 510 nm, the self-prepared sample showed decay with a longer life time than the decay time for UV100. The decay kinetics of the photogenerated charge carriers could be fitted by second order reaction kinetics according to the Eq. 10.

$$\Delta J(t) = \frac{J_0}{K_r J_0 t + 1} \quad (10)$$

A rate constant  $K_r$  values of  $10.9 \times 10^{-7}$  and  $1.74 \times 10^{-7}$  (s%)<sup>-1</sup> for UV100 and S5, respectively have been obtained evincing improved charge carrier separation in the prepared material even in the absence of any electron donor. Thus, in the presence of suitable electron donors, the electrons are available for an extended period to induce reduction reactions. Such phenomena has been assigned to the surface defects that enable the capture the electrons and suppress the recombination of electrons and holes [38], and could in turn facilitate the migration of charge carriers to the surface due to the slower charge carrier recombination. To sum up the observations of this section, a higher concentration and a longer life time of the photogenerated charge carriers in the prepared samples have been obtained, as well as a broad distribution of trapped states, acting most likely as surface defect sites.

#### 4. Conclusions

We successfully applied the design of experiment approach combined with full factorial design to investigate the most influential variable affecting the preparation of TiO<sub>2</sub> through EISA method. TiCl<sub>3</sub> is the decisive factor that maximizes the photocatalytic hydrogen evolution. Combining TiCl<sub>3</sub> as a precursor with F-108 as a surfactant leads to the formation of pure anatase TiO<sub>2</sub> characterized by its response to the visible light in addition to its unexpected photocatalytic activity towards the hydrogen evolution in absence of any co-catalyst. The higher photocatalytic activity could be related to the band edge positions and the higher charge carrier density that facilitates the transport of charge carrier. The wider distribution of energetically different trapping sites for the holes increases the adsorption sites and accelerates their reactions with adsorbates; hence the synthesised material could be used as a photocatalyst in a promising environmental-friendly technique aiming to the generation of renewable energy source. Future study will be done to explain the photocatalytic activity of the prepared material towards the evolution of hydrogen gas. Finally, in order to demonstrate the viability of semiconductor photocatalysis to be scaled-up for environmental remediation and energy conversion, several technical and economical factors, which are related to reactor design, should be considered. These factors include the uniform distribution of illumination and photocatalytic particulates as well as reaction kinetics. The issue of providing sufficient specific surface area of catalyst and effective photocatalyst illumination are particularly important in this area. The simplicity of the preparation method and the possibility to produce molecular hydrogen without using a co-catalyst are an opportunity to scale-up the manufacturing such photocatalysts for large scale reactors towards an economic commercial distribution. Scaling up of the photocatalyst synthesis developed herein should be feasible, both technically and economically. It will, however, require appropriate technical equipment, which currently are not available in the authors' laboratory.

## Acknowledgements

The financial support from the Deutscher Akademischer Austauschdienst (DAAD) and the Federal Foreign Office is gratefully acknowledged. This Special Issue is dedicated to honor the retirement of Dr. John Kiwi at the Swiss Federal Institute of Technology (Lausanne), a key figure in the topic of photocatalytic materials for the degradation of contaminants of environmental concern.

## Appendix A. Supplementary data

Supplementary material related to this article can be found, in the online version, at doi:<https://doi.org/10.1016/j.apcatb.2018.07.045>.

## References

- [1] A. Hakki, et al., Hydrogen production by heterogeneous photocatalysis, in: K. Wandelt (Ed.), Encyclopedia of Interfacial Chemistry, Elsevier, Oxford, 2018, pp. 413–419.
- [2] Y. AlSalka, et al., Understanding the degradation pathways of oxalic acid in different photocatalytic systems: towards simultaneous photocatalytic hydrogen evolution, *J. Photochem. Photobiol. A* (2018).
- [3] E. Friehs, et al., Toxicity, phototoxicity and biocidal activity of nanoparticles employed in photocatalysis, *J. Photochem. Photobiol. C* 29 (2016) 1–28.
- [4] A. Fujishima, K. Honda, Electrochemical photolysis of water at a semiconductor electrode, *Nature* 238 (5358) (1972) 37–38.
- [5] E. Masolo, et al., Mesoporous titania powders: the role of precursors, ligand addition and calcination rate on their morphology, crystalline structure and photocatalytic activity, *Nanomaterials* 4 (3) (2014) 583.
- [6] Y. Wan, Zhao, On the controllable soft-templating approach to mesoporous silicates, *Chem. Rev.* 107 (7) (2007) 2821–2860.
- [7] V. Etacheri, et al., Visible-light activation of TiO<sub>2</sub> photocatalysts: advances in theory and experiments, *J. Photochem. Photobiol. C* 25 (2015) 1–29.
- [8] X. Pan, et al., Defective TiO<sub>2</sub> with oxygen vacancies: synthesis, properties and photocatalytic applications, *Nanoscale* 5 (9) (2013) 3601–3614.
- [9] H. Yang, et al., Free-standing and oriented mesoporous silica films grown at the air-water interface, *Nature* 381 (6583) (1996) 589–592.
- [10] C.J. Brinker, et al., Evaporation-induced self-assembly: nanostructures made easy, *Adv. Mater.* 11 (7) (1999) 579–585.
- [11] L. Mahoney, R. Koodali, Versatility of evaporation-induced self-assembly (EISA) method for preparation of mesoporous TiO<sub>2</sub> for energy and environmental applications, *Materials* 7 (4) (2014) 2697.
- [12] J.H. Pan, X.S. Zhao, W.I. Lee, Block copolymer-templated synthesis of highly organized mesoporous TiO<sub>2</sub>-based films and their photoelectrochemical applications, *Chem. Eng. J.* 170 (2) (2011) 363–380.
- [13] J. Zhang, et al., Ligand-assisted assembly approach to synthesize large-pore ordered mesoporous titania with thermally stable and crystalline framework, *Adv. Energy Mater.* 1 (2) (2011) 241–248.
- [14] D. Grosso, et al., Fundamentals of mesostructuring through evaporation-induced self-assembly, *Adv. Funct. Mater.* 14 (4) (2004) 309–322.
- [15] E.L. Crepaldi, et al., Controlled formation of highly organized mesoporous titania thin films: from mesostructured hybrids to mesoporous nanoanatase TiO<sub>2</sub>, *J. Am. Chem. Soc.* 125 (32) (2003) 9770–9786.
- [16] G.J.d.A.A. Soler-Illia, C. Sanchez, Interactions between poly(ethylene oxide)-based surfactants and transition metal alkoxides: their role in the templated construction of mesostructured hybrid organic-inorganic composites, *New J. Chem.* 24 (7) (2000) 493–499.
- [17] P. Yang, et al., Block copolymer templating syntheses of mesoporous metal oxides with large ordering lengths and semicrystalline framework, *Chem. Mater.* 11 (10) (1999) 2813–2826.
- [18] H. Luo, C. Wang, Y. Yan, Synthesis of mesostructured titania with controlled crystalline framework, *Chem. Mater.* 15 (20) (2003) 3841–3846.
- [19] C.-C. Sung, et al., Synthesis of highly ordered and worm-like mesoporous TiO<sub>2</sub> assisted by tri-block copolymer, *Solid State Ionics* 179 (27) (2008) 1300–1304.
- [20] F. Bosc, et al., Mesostructure of anatase thin films prepared by mesophase templating, *Chem. Mater.* 16 (11) (2004) 2208–2214.
- [21] G.J.d.A.A. Soler-Illia, et al., Chemical strategies to design textured materials: from microporous and mesoporous oxides to nanonetworks and hierarchical structures, *Chem. Rev.* 102 (11) (2002) 4093–4138.
- [22] K. Cassiers, et al., Surfactant-directed synthesis of mesoporous titania with nanocrystalline anatase walls and remarkable thermal stability, *J. Phys. Chem. B* 108 (12) (2004) 3713–3721.
- [23] N.D. Stanley, L.M. Stephen, Chapter 10 an example of regression analysis on existing data, *Data Handling in Science and Technology*, Elsevier, 1993, pp. 177–197.
- [24] Y. AlSalka, F. Karabet, S. Hashem, Development and optimisation of quantitative analytical method to determine BTEX in environmental water samples using HPLC-DAD, *Anal. Methods* 2 (8) (2010) 1026–1035.
- [25] Y. AlSalka, F. Karabet, S. Hashem, Evaluation of electrochemical processes for the removal of several target aromatic hydrocarbons from petroleum contaminated water, *J. Environ. Monit.* 13 (3) (2011) 605–613.
- [26] L. Chen, et al., Synthesis of well-ordered mesoporous titania with tunable phase content and high photoactivity, *J. Phys. Chem. C* 111 (32) (2007) 11849–11853.
- [27] A. Hakki, et al., Hydrogen Production by Heterogeneous Photocatalysis A2 - Wandelt, Klaus, Encyclopedia of Interfacial Chemistry, Elsevier, Oxford, 2018, pp. 413–419.
- [28] R.W. Mee, Analysis of Full Factorial Experiments, in A Comprehensive Guide to Factorial Two-Level Experimentation, Springer New York, New York, NY, 2009, pp. 27–74.
- [29] P. Brandani, P. Stroeve, Kinetics and equilibria of adsorption of peo<sup>n</sup>ppo<sup>n</sup>PEO triblock copolymers on a hydrophilic self-assembled monolayer on gold, *Macromolecules* 37 (17) (2004) 6640–6643.
- [30] V. Shah, et al., Correlation of dynamic surface tension with sedimentation of PTFE particles and water penetration in powders, *Langmuir* 31 (51) (2015) 13725–13733.
- [31] R. López, R. Gómez, Band-gap energy estimation from diffuse reflectance measurements on sol-gel and commercial TiO<sub>2</sub>: a comparative study, *J. Sol-Gel Sci. Technol.* 61 (1) (2012) 1–7.
- [32] J. Schneider, et al., Improved charge carrier separation in barium tantalate composites investigated by laser flash photolysis, *PCCP* 18 (16) (2016) 10719–10726.
- [33] F. Sieland, J. Schneider, D.W. Bahnemann, Fractal charge carrier kinetics in TiO<sub>2</sub>, *J. Phys. Chem. C* 121 (43) (2017) 24282–24291.
- [34] R.L. Cordell, et al., GC-MS analysis of ethanol and other volatile compounds in micro-volume blood samples: quantifying neonatal exposure, *Anal. Bioanal. Chem.* 405 (12) (2013) 4139–4147.
- [35] J. Ab Rahman, Analysing Research Data, in Brief Guidelines for Methods and Statistics in Medical Research, Springer Singapore, Singapore, 2015, pp. 35–101.
- [36] V.A. Cheng, L.M. Walker, Transport of nanoparticulate material in self-assembled block copolymer micelle solutions and crystals, *Faraday Discuss.* 186 (0) (2016) 435–454.
- [37] S.E. Braslavsky, et al., Glossary of terms used in photocatalysis and radiation catalysis (IUPAC recommendations 2011), *Pure Appl. Chem.* 83 (4) (2011) 931–1014.
- [38] W. Zhijiao, et al., Effects of bulk and surface defects on the photocatalytic performance of size-controlled TiO<sub>2</sub> nanoparticles, *Nanotechnology* 28 (27) (2017) p. 275706.
- [39] M. Kong, et al., Tuning the relative concentration ratio of bulk defects to surface defects in TiO<sub>2</sub> nanocrystals leads to high photocatalytic efficiency, *J. Am. Chem. Soc.* 133 (41) (2011) 16414–16417.
- [40] A.V. Puga, et al., Production of H<sub>2</sub> by ethanol photoreforming on Au/TiO<sub>2</sub>, *Adv. Funct. Mater.* 24 (2) (2014) 241–248.
- [41] J. Schneider, D.W. Bahnemann, Undesired role of sacrificial reagents in photocatalysis, *J. Phys. Chem. Lett.* 4 (20) (2013) 3479–3483.
- [42] R. Gao, A. Safrany, J. Rabani, Fundamental reactions in TiO<sub>2</sub> nanocrystallite aqueous solutions studied by pulse radiolysis, *Radiat. Phys. Chem.* 65 (6) (2002) 599–609.
- [43] F. Amano, et al., Effect of Ti<sup>3+</sup> ions and conduction band electrons on photocatalytic and photoelectrochemical activity of rutile titania for water oxidation, *J. Phys. Chem. C* 120 (12) (2016) 6467–6474.
- [44] M.C. Sanchez-Sanchez, et al., Mechanistic aspects of the ethanol steam reforming reaction for hydrogen production on Pt, Ni, and PtNi catalysts supported on Ti<sup>3+</sup>-Al<sub>2</sub>O<sub>3</sub>, *J. Phys. Chem. A* 114 (11) (2010) 3873–3882.
- [45] L.V. Mattos, et al., Production of hydrogen from ethanol: review of reaction mechanism and catalyst deactivation, *Chem. Rev.* 112 (7) (2012) 4094–4123.
- [46] R. Li, et al., Achieving overall water splitting using titanium dioxide-based photocatalysts of different phases, *Energy Environ. Sci.* 8 (8) (2015) 2377–2382.
- [47] Y.K. Kho, et al., Photocatalytic H<sub>2</sub> evolution over TiO<sub>2</sub> nanoparticles. The synergistic effect of anatase and rutile, *J. Phys. Chem. C* 114 (6) (2010) 2821–2829.
- [48] N. Liu, et al., Hydrogenated anatase: strong photocatalytic dihydrogen evolution without the use of a Co-catalyst, *Angew. Chem. Int. Ed.* 53 (51) (2014) 14201–14205.
- [49] K.S.S. Sing, Reporting Physisorption Data for Gas/Solid Systems With Special Reference to the Determination of Surface Area and Porosity, Brunel University, UK, 1982, pp. 2201–2218.
- [50] W. Li, et al., A perspective on mesoporous TiO<sub>2</sub> materials, *Chem. Mater.* 26 (1) (2014) 287–298.
- [51] Y. Ren, Z. Ma, P.G. Bruce, Ordered mesoporous metal oxides: synthesis and applications, *Chem. Soc. Rev.* 41 (14) (2012) 4909–4927.
- [52] L.-B. Xiong, et al., In the surface of titanium dioxide: generation, properties and photocatalytic application, *J. Nanomat.* 2012 (2012) 13.
- [53] M. Wen, et al., In situ synthesis of Ti<sup>3+</sup> self-doped mesoporous TiO<sub>2</sub> as a durable photocatalyst for environmental remediation, *Chin. J. Catal.* 36 (12) (2015) 2095–2102.
- [54] X. Zhang, et al., Facile synthesis and enhanced visible-light photocatalytic activity of Ti<sup>3+</sup>-doped TiO<sub>2</sub> sheets with tunable phase composition, *Front. Chem. Sci. Eng.* 9 (3) (2015) 349–358.
- [55] S.K. Cushing, et al., Effects of defects on photocatalytic activity of hydrogen-treated titanium oxide nanobelts, *ACS Catal.* 7 (3) (2017) 1742–1748.
- [56] L. Kavan, et al., Electrochemical and photoelectrochemical investigation of single-crystal anatase, *J. Am. Chem. Soc.* 118 (28) (1996) 6716–6723.
- [57] R. Beranek, (Photo)electrochemical methods for the determination of the band Edge positions of TiO<sub>2</sub>-based nanomaterials, *Adv. Phys. Chem.* 2011 (2011) 20.
- [58] S. Wang, et al., Titanium-defected undoped anatase TiO<sub>2</sub> with p-type conductivity, room-temperature ferromagnetism, and remarkable photocatalytic performance, *J. Am. Chem. Soc.* 137 (8) (2015) 2975–2983.
- [59] Z. Chen, H. Dinh, E. Miller, Photoelectrochemical Water splitting. Standards, experimental methods, and protocols, SpringerBriefs in Energy, 1 ed., Springer-Verlag, New York, 2013, p. 126.
- [60] Q. Kang, et al., Reduced TiO<sub>2</sub> nanotube arrays for photoelectrochemical water

- splitting, *J. Mater. Chem. A* 1 (18) (2013) 5766–5774.
- [61] M. Mehta, et al., Hydrogen treated anatase TiO<sub>2</sub>: a new experimental approach and further insights from theory, *J. Mater. Chem. A* 4 (7) (2016) 2670–2681.
- [62] Y. Murakami, et al., Femtosecond diffuse-reflectance spectroscopy of various commercially available TiO<sub>2</sub> powders, *Spectrosc. Lett.* 44 (2) (2011) 88–94.
- [63] X. Wang, et al., Transient absorption spectroscopy of anatase and rutile: the impact of morphology and phase on photocatalytic activity, *J. Phys. Chem. C* 119 (19) (2015) 10439–10447.
- [64] Y. Tamaki, et al., Direct observation of reactive trapped holes in TiO<sub>2</sub> undergoing photocatalytic oxidation of adsorbed alcohols: evaluation of the reaction rates and yields, *J. Am. Chem. Soc.* 128 (2) (2006) 416–417.
- [65] D.W. Bahneemann, M. Hilgendorff, R. Memming, Charge carrier dynamics at TiO<sub>2</sub> particles: reactivity of Free and trapped holes, *J. Phys. Chem. B* 101 (21) (1997) 4265–4275.
- [66] B. Ohtani, Titania photocatalysis beyond recombination: a critical review, *Catalysts* 3 (4) (2013) 942.